CHEMISTRY
A European Journal

A Journal of
ChemPubSoc Europe

Accepted Article

Title: Defects Promoting Ultrafast Charge Separation in Graphitic Carbon Nitride Enhanced Visible-Light-Driven CO2 Reduction Activity

Authors: Hainan Shi, Saran Long, Jungang Hou, Lu Ye, Yanwei Sun, Wenjun Ni, Chunshan Song, Keyan Li, Gagik G. Gurzadyan, and Xinwen Guo

To be cited as: *Chem. Eur. J.* 10.1002/chem.201805923

Link to VoR: http://dx.doi.org/10.1002/chem.201805923

Supported by
ACES

WILEY-VCH

Defects Promoting Ultrafast Charge Separation in Graphitic Carbon Nitride Enhanced Visible-Light-Driven CO_2 Reduction Activity

Hainan Shi,[a] Saran Long,[a] Jungang Hou,*[a], Lu Ye,[a] Yanwei Sun,[a] Wenjun Ni,[a] Chunshan Song,[a,b] Keyan Li,*[a], Gagik G.Gurzadyan[a] and Xinwen Guo*[a]

Dedication (optional)

Abstract: The fundamental photocatalytic limitations for solar CO_2 reduction remain due to low efficiency, serious charge recombination and short lifetime of catalysts. Herein, as a prototype, two-dimensional graphitic carbon nitride nanosheets with nitrogen vacancies (g-C_3N_x) located at both tricoordinated N atoms and uncondensed terminal NH_x species were prepared by one-step tartaric acid assistant thermal polymerization of dicyandiamide. Transient absorption spectra results revealed that the defects in the g-C_3N_4 acted as the trapped states of charges resulting into the prolonged lifetimes of charge carrier photoexcited. Time-resolved photoluminescence spectra analysis ensured that the faster decay of charges was due to the decreased layer stacking distance in the g-C_3N_x in favor of hopping transition and mobility of charge carriers to surface of materials. Benefiting from the synergic virtues of strong visible-light absorption, large surface area as well as efficient charge separation, the g-C_3N_x nanosheets with negligible loss after 15 h photocatalysis exhibited CO evolution rate of 56.9 μmol g^{-1} h^{-1}, roughly 8 times higher than that of pristine g-C_3N_4 under visible light irradiation. This work presents the role of defects in modulating light absorption, charge separation, opening an avenue enabling robust solar energy conversion performances.

Introduction

Over-consumption of finite fossil fuels not only breaks out energy crisis but also brings out environmental issue related to CO_2 atmosphere progressive increase, both of which will impose restriction on society sustainable development and human survival in the long run.[1] CO_2 converted into chemicals driven by solar energy provides an attractive and promising way to address global energy demands and alleviate climate change.[2] Ever since Inoue et al.[3] reported the photoelectrocatalytic reduction of CO_2 conducted by semiconductors in aqueous solution, the photocatalytic conversion of CO_2 into fuels has attracted much attention.[4] However, the CO_2 reduction reaction itself is a much complex process, involving multiple electrons and protons coupling resulting into several different reaction pathways, and thus leading to many possible final products.[2c, 5] In addition, most of materials applied to CO_2 reduction require a large over-potential, which gives rise to the limit of materials choice and the low turnover rate of CO_2 reduction product. Therefore, it is of great importance to design a high-performance CO_2 photoreducion catalyst to cater for technological development.

Among catalysts, graphitic carbon nitride (g-C_3N_4) has been extensively explored as a heterogeneous metal-free semiconductor photocatalyst due to its earth-abundance, nontoxicity, facile synthesis, good stability, as well as a suitable bandgap.[6] However, the pristine g-C_3N_4 suffers from the low surface area, rapid recombination rate of photoexcited charge carriers and unsatisfied visible light absoprtion, leading to the poor photocatalytic activity. Great efforts have been made to solve these problems, such as doping with heteroatoms (metal[7] or non-metal[8] atom), introducing defects,[9] decorating with function groups,[10] constructing ordered porous structure,[11] and controlling morphology.[12] It is reported that the intrinsic defects that usually generated a mid-gap state as a band tail state can play the role of the trapping sites for photoexcited carriers, consequently boosting the photocatalytic activity.[13] Recently, mamy strategies of bulding nitrogen vacancies in g-C_3N_4 have been widely investigated for enhancing the photocatalytic activity including controlling the polycondensation temperature,[14] hydrothermal treatment,[15] alkali-assisted thermal polymerization[16] and hydrogen reduction.[17] Acid-treament of g-C_3N_4 or its precusor such as using HNO_3,[18] HCl,[9a] H_2SO_4[19] and H_3PO_4[20] is also an efficient method to produce defects. Tartaric acid (TA) is a weak acid without heteroatom except C, H and O atoms. In addition, it will react with amino in the precusor of g-C_3N_4 to form supermolecule in the aqueous solution. Meanwhile, TA will completely decompose into CO_2 and H_2O in high temperature, which might lead to defects forming during the thermal treament. Inspired of these merits and defect engineering, it is desirable to explore a facile approach to produce defective g-C_3N_4 using TA to enhance photocatalytic activity. In addition, it is of great interest to investigate the truth of the charge separation dynamics of the nitrogen defects in the g-C_3N_4 and relationship between charge seapariton and photoreduction CO_2 activity,

---

[a] H. Shi, Dr. S. Long, Dr. J. Hou, Dr. L. Ye, Y. Sun, W. Ni, Dr. C. Song, Dr. K. Li, Dr. G. Gurzadyan, Dr. X. Guo
State Key Laboratory of Fine Chemicals, PSU-DUT Joint Center for Energy Research
School of Chemical Engineering
Dalian University of TechnologyDalian 116024, P. R. China.
Dalian 116024, P. R. China.
E-mail: guoxw@dlut.edu.cn; jhou@dlut.edu.cn; keyanli@dlut.edu.cn
[b] Dr. C. Song Department
EMS Energy Institute, PSU-DUT Joint Center for Energy Research and Department of Energy & Mineral Engineering, Pennsylvania State university
University Park, Pennsylvania 16802, United States

Supporting information for this article is given via a link at the end of the document.

presenting in-depth understanding of the photocatalytic mechanism.

To resolve the limitations of low efficiency, serious charge recombination and short lifetime of catalysts, two-dimensional graphitic carbon nitride nanosheets with nitrogen vacancies (g-C_3N_x) located at both tricoordinated N atoms and uncondensed terminal NH_x species were prepeard by one-step tartaric acid assistant thermal polymerization of dicyandiamide. Transient absorption spectra results revealed the defects in the g-C_3N_4 result in the prolonged photoexcited charge carrier lifetimes and acted as the trapped states of charges to promote charge separation. Time-resolved photo-luminescence spectra analysis ensured the faster decay of charges was due to the decreased layer stacking distance in g-C_3N_x in favor of hopping transition and mobility of charge carriers to surface of materials. Benefiting from the synergic virtues of enhanced visible light absorption, abundant active sites and efficient charge separation and transfer as well as prolonged charge lifetimes, defective g-C_3N_x nanosheets with negligible loss after 15 h photocatalysis exhibited CO formation rate of 56.9 μmol g^{-1} h^{-1}, roughly 8 times higher than that of pristine g-C_3N_4 under visible light irradiation. This work provides insight into design and preparation of high performance g-C_3N_4 based photocatalysts.

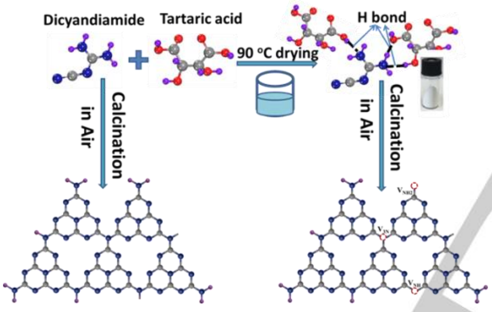

Scheme 1. Illustration of synthesis of DCN-x by hydrogen bond induced supramolecular assembly. (C, N, O and H atoms are indicated by gray, blue, red and purple spheres, respectively.)

Results and Discussion

Two-dimensional graphitic carbon nitride nanosheets with nitrogen vacancies (g-C_3N_x) located at both tricoordinated N atoms and uncondensed terminal NH_x species were prepared by one-step tartaric acid (TA) assistant thermal polymerization of dicyandiamide (D) (Scheme 1). The crystal structure of pristine g-C_3N_4 (DCN) and a series of DCN-*x* samples were characterized by XRD patterns and FT-IR spectroscopy. As shown in Figure 1a, DCN exhibits two distinct diffraction peaks at 13.1° and 27.4°, which are attributed to in-plane packing of tri-s-triazine motifs (100 plane) and layered interfacial stacking of the conjugated tri-s-triazine structure (002 plane), respectively.[21] DCN-*x* samples show the similar XRD patterns with DCN, suggesting that DCN-*x* have the same structure with g-C_3N_4. Furthermore, it is observed that the (100) peak gradually becomes broadened when TA was introduced into the reaction system (Figure 1b), resulting from the less ordered stacking of tri-s-triazine motifs.[22] This may arise from the formation of nitrogen vacancies or the substitution of C or N with O in the structure of tri-s-triazine motifs.[4] Remarkably, the slight shift of 27.4° peak to higher 2 θ increases with TA usage as shown in Figure 1b, indicating the smaller layered interfacial stacking distance. Furthermore, this peak gradually weakens with TA amount, demonstrating the loss of ordered structures within the framework caused by defects generated during the thermal-polymerization process. This can be further explained by the results of XRD patterns and FT-IR spectra of solid mixture of TA and D (Figure S1 and S2, Supporting Information). The strongest peak located at 26.3° weakens and the weaker peaks at 26.7° and 28.2° became stronger in XRD patterns, while the positions of main diffraction peaks in XRD patterns and FT-IR spectra remains unchanged. These phenomena implie that TA interacts with D through hydrogen bond and ionic bond. The interaction by hydrogen bond between both precursors finally results in the decrease of layered interfacial distance. Furthermore, the weight loss speed of 0.05TA-D is slower than D after 300°C in the TG curves, which demonstrates that the interaction between TA and D alleviates the sublimation and accelerates condensation process thus resulting in structure change (Figure S3).

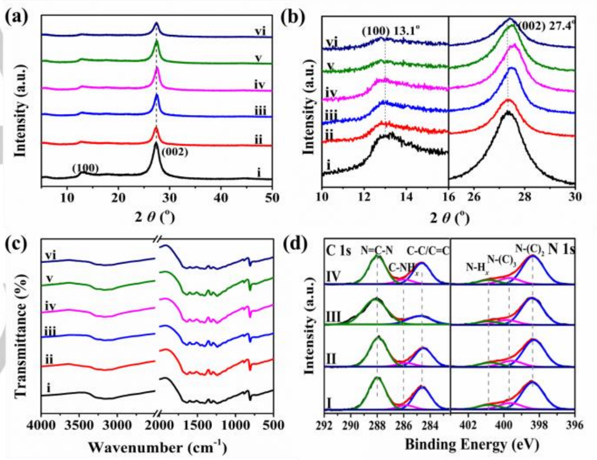

Figure 1. (a, b) XRD patterns, (c) FT-IR spectra of DCN and DCN-x. i-vi represents DCN, DCN-0.01, DCN-0.025, DCN-0.05, DCN-0.075 and DCN-0.1. (d) High-resolution C1s, N1s XPS spectra of DCN and DCN-x. I-IV represent DCN, DCN-0.01, DCN-0.05 and DCN-0.1.

Based on the analysis of FT-IR spectra for the bonding structures of DCN-*x*, the main molecular structure of g-C_3N_x was almost unchanged through TA assistant synthesis of g-C_3N_4. As shown in Figure 1c, the peaks located at 810 cm^{-1} and 1200-1800 cm^{-1} are ascribed to breathing vibration of heptazine rings out-plane and skeletal vibrations of aromatic N−CN heterorings, respectively. The bands appeared at 3000-3500 cm^{-1} region correspond to N–H stretching vibration.[23] To further investigate the chemical state and surface elemental composition of DCN-*x*, XPS and elemental analysis were performed. The very small O1s peaks in the XPS survey spectra are due to the surface adsorbed oxygen-containing species such as water (Figure S4). The C1s XPS spectra for the pristine g-C_3N_4 and DCN-*x* contain three kinds of C species located at 284.6, 286.0 and 288.0 eV, corresponding to the sp^2 hybrid orbital of adventitious carbon C−C/C=C, C−NH_x bond on the edges of heptazine units, and the sp^2 hybrid orbital of N=C−N species in the s-triazine ring of g-C_3N_4, respectively (Figure 1d). Remarkably, the area of the peak located at 286.0 eV for DCN-0.05 is much smaller compared with other samples, which indicates the content of C−NH_x species in DCN-0.05 is lower. The N1s XPS spectra (Figure 1d) for the DCN and DCN-*x* show three peaks at 398.4, 399.7 and 401.0 eV, assigned to bicoordinated N atom (N−$(C)_2$), tricoordinated N atom (N−$(C)_3$) and surface amino groups (N−H_x), respectively. The ratio of $N_{(2C)}/N_{(3C)}$ and $N_{(2C)}/NH_x$ of DCN-*x* calculated by XPS N1s spectra (Table S1) increases compared with DCN, indicating the formation of nitrogen vacancies via the departure of $N_{(3C)}$ and NH_x species in the process of TA and D co-polymerization.[24] Therefore, the DCN-*x* are rich in N defects loacted at both tricoordinated N atoms and uncondensed terminal NH_x species. Moreover, N defects formation in the DCN-*x* was further comfirmed by elemental analysis (Table S1).[16, 24b, 25] Combined with the results of XPS and elemental analysis, DCN-0.05 with the highest ratio of $N_{(2C)}/N_{(3C)}$ and $N_{(2C)}/N\text{-}H_x$ shows the highest concentration of the surface N defects. And the total N defects in the DCN-*x* increase with increasing of TA amount.

Table 1. Specific surface areas, pore volume, band gap derived from the transformed Kubelka–Munk function and photocatalytic performance of the samples.

Sample	S_{BET} ($m^2 g^{-1}$)	V_{total} ($cm^3 g^{-1}$)	E_g (eV)	Yield ($\mu mol\ g^{-1}$)		Sel. (%)
				CO	H_2	CO
DCN	10.0	0.037	2.70	35.5	5.9	85.7
DCN-0.01	14.4	0.046	2.60	240.2	30.1	88.9
DCN-0.025	19.3	0.059	2.56	251.1	48.3	83.9
DCN-0.05	29.5	0.076	2.49	284.7	51.6	84.7
DCN-0.075	16.8	0.051	2.40	186.1	31.5	85.5
DCN-0.1	15.9	0.043	2.24	119.3	16.1	88.1

It is well known that the specific surface area and porosity volume of the photocatalysts are crucial factors for the photocatalytic reaction performance. N_2 adsorption-desorption isotherms of the pristine g-C_3N_4 and g-C_3N_x exhibit the type IV-H_3 type hysteresis loops, indicating the existence of the mesopores (Figure S5). Obviously, DCN has the lowest N_2 adsorption volume while DCN-0.05 displays the highest one. As listed in Table 1, the specific surface area and pore volume of DCN-*x* samples are larger than that of DCN (10.0 $m^2 g^{-1}$, 0.037 $cm^3 g^{-1}$), and increase progressively from DCN-0.01 to DCN-0.05 and then decrease. DCN-0.05 shows the largest specific surface area (29.5 $m^2 g^{-1}$) and pore volume (0.076 $cm^3 g^{-1}$), which are both larger than those of DCN, respectively. Surface area and pore volume increased may be concerned with the morphology change. Scanning electron microscopy (SEM) images of DCN-0.05 (Figure S6a) display a curly sheet-like structure in smaller sizes, even no longer bulk-shaped as DCN (Figure S6c, d). Furthermore, transmission electron microscopy (TEM) and high-angle annular dark field STEM (HAADF-STEM) images further confirm that DCN-0.05 possesses the curly nanosheets shape (Figure S6b and Figure 2b). To conduct the component, the energy dispersive X-ray (EDX) elemental mapping images reveal that C and N elements are homogenously distributed (Figure 2c,d). Based on above-mentioned analysis, the morphology change from bulk to nanosheets could be attributed to the release of gas by TA decomposition during the thermal-polymerization resulting in the volume expansion of the catalyst, thus leading to the increase of specific surface area and pore volume.

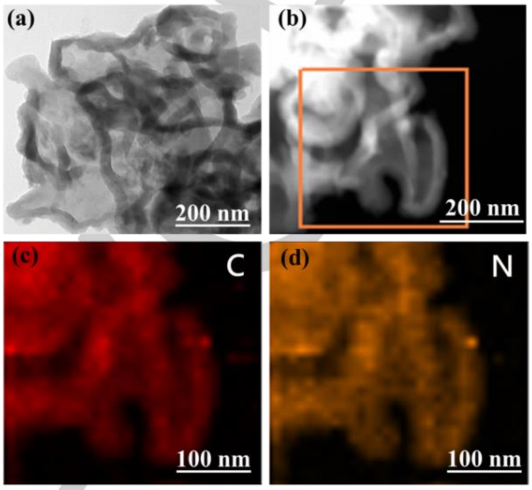

Figure 2. (a) TEM image. (b) HAADF-STEM image. (c, d) elemental mapping for of DCN-0.05.

It is rather remarkable that the color of DCN-*x* changed from yellow to deep brown with the increase of TA amount (Figure S7). After the optical analysis by UV-vis diffuse reflectance spectroscopy (Figure 3a), the strong absorption tail in the visible light region is observed for the DCN-*x*. The band gap structures by transformed Kubelka–Munk function are shown in Figure 3b and in Table 1. The variation of band gap for DCN-*x* is narrowed with increasing of TA amount. The second band gaps are also observed in the DCN-*x* and gradually narrowed from 2.02 eV to 1.70 eV. The apparently decreased band gaps could be ascribed to the nitrogen vacancies, which not only have enhanced the visible light absorption but also introduced a defect level and modified the electron structure of the g-C_3N_4.[24b] To further elaborate the band gap of DCN-*x*, the valance band (VB) position was collected by XPS spectra (Figure S8). As shown in Figure S8, all DCN-x exhibit similar VB maximum compared with DCN (VB ≈ 1.50 eV). The contact potential difference between the samples and the analyzer was estimated to be ≈ 1.66 V versus normal hydrogen electrode (NHE) using the formula $E_{NHE}/V = \Phi + 1.50\ eV - 4.44$ (E_{NHE}: potential of normal hydrogen electrode; Φ of 4.60 eV: the electron work function of the analyzer).[15-16, 26] The result suggests that the VB position has not been affected by the nitrogen vacancies in the framework of g-C_3N_4. However, the conduction band (CB) has an obvious decrease on the basis of the narrow band gap. The gradual narrowing second band gap is contributed to N defects in DCN-*x*, i.e. it is directly proportional to N defects content. The proposal of CB, VB and defect level positions in detail is drawn in the Figure 3c. It can be seen that the defect levels of DCN-x are below the CB with gradual lower position. Furthermore, the location of defect levels for the DCN-

10.1002/chem.201805923

0.075 and DCN-0.1 is −0.06 and −0.04 eV, respectively, and below the potential of CO_2 reduced to CO (−0.07 eV), which is disadvantageous to photocatalytic reaction for CO_2 to CO.

The formation of nitrogen vacancies in the DCN-*x* samples may also influence the separation efficiency of charge. As shown in Figure 3d, the steady photoluminescence (PL) spectrum for pristine g-C_3N_4 shows a high intensity fluorescence signal at 400-580 nm. The gradual decrease of signal intensity for the nitrogen deficient g-C_3N_4 indicates that the recombination of the photoinduced electrons and holes is substantially suppressed. Especially, the lowest intensity for the DCN-0.1, implies the superior separation efficiency of charge carriers.

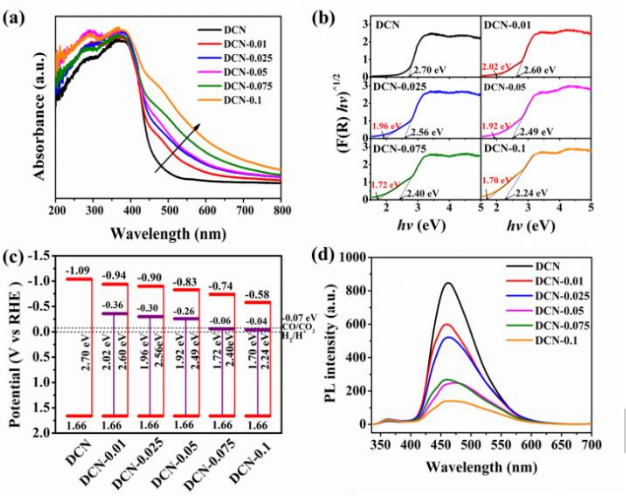

Figure 3. (a) UV-Vis diffuses reflectance spectra. (b) Plots of transformed Kubelka–Munk function versus photon energy. (c) Band structure alignments and (d) steady PL spectra for DCN and DCN-x.

Based on unique physicochemical characteristics of defective g-C_3N_x nanosheets, it is essential to evaluate the photocatalytic CO_2 reduction performance. At the initial stage, no products were detected without either photocatalyst or light source and even without the introduction of CO_2 under light irradiation As shown in Figure 4a and Figure S9, all of DCN-*x* exhibit excellent photocatalytic CO_2 reduction activity compared with DCN. The photocatalytic activity firstly increased and then deceased rapidly from DCN-0.05 to DCN-0.1. It is noted that the superior photocatalyic activity of the DCN-0.05 could be attributed to its larger specific surface area and pore volume, enhanced light absorption and better charge separation efficiency caused by N defects. However, the deceased performance for the DCN-0.075 and DCN-0.1 can be explained by the position for defect levels (−0.06 and −0.04 eV) lower than the potencial (−0.07 eV) of the photocatalytic CO_2 into CO. Besides, the CO evolution rate, 284.7 μmol g^{-1} on DCN-0.05 with the selectivity of approximate 90% was nearly eight times higher than that of the pristine g-C_3N_4 (35.5 μmol g^{-1}), corresponding a small amounts of H_2 products (Figure 4b and Table 1) under 5 h visible-light irradiation. For the practical application, the stability is a pivot role for the photocatalyst. No obvious decrease is observed in three cycles for CO evolution rate of DCN-0.05 (Figure 4c). From XRD patterns and FT-IR spectra of used catalyst (Figure S10), the basic framework of g-C3N4 still remains for the used photocatalyst. SEM images of used photocatalyst also disclose that used catalyst still maintains nannsheets-like morphology (Figure S11). The results above demonstrate the high stability of the catalysts.

To analyze the reasons of the enhanced photocatalytic activities of DCN-*x,* the EPR and photoelectrochemical mesurements were explored. DCN-0.05 as well as DCN display a paramagnetic absorption signal with a g value of 2.003, which is assigned to the unpaired electron localized at the carbon atom in a typical heptazine of g-C_3N_4 (Figure S12).[24b, 27] The stronger peak signal of DCN-0.05 is attributed the formation of nitrogen vacancies, leading to the increased amount of unpaired electrons as the active sites for solar CO_2 reduction.[28] Transient photocurrent measurements of DCN and DCN-0.05 show a sensitive photocurrent response during on/off visible light irradiation cycles (Figure S13). Compared with DCN, the higher photocurrent response for DCN-0.05 indicates more efficient charge carrier separation and transportation rate in deficient g-C_3N_4. From the EIS tests (Figure S14), a smaller arc radius for DCN-0.05 is observed, further indicating the faster charge transportation and better charge carrier separation for DCN-*x* compared with DCN.

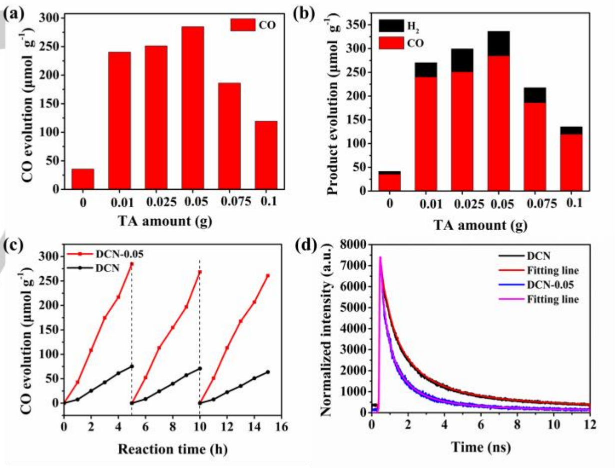

Figure 4. (a, b) CO evolution and CO and H_2 distribution for DCN and DCN-x. (c) Time courses of CO evolution of DCN-0.05. (d) Time-resolved photoluminescence decay spectra of DCN and DCN-0.05 probed at 500 nm by time-correlated single-photon counting. The samples were excited by incident light of 400 nm from a picosecond pulsed light emitting diode.

To further clarify the in-depth understanding of charge separation dynamics, time-resolved photoluminescence (tr-PL) and transient absorption (TA) spectroscopies were investigated systematically. The fluorescence lifetime of charge carriers by time-correlated single photon counting (TCSPC) has been shown in Figure 4d. Both spectra show multi-exponential decays and the overall decay of DCN-0.05 is faster than that of DCN.

Table 2 Decay lifetimes of tr-PL, fs-TA and ns-TA spectra and their relative amplitude of photoexcited charge carriers in the g-C_3N_4 and nitrogen-deficient g-C_3N_4.

Method	Sample	λ[a], nm	τ_1[b]	A_1[c]	τ_2	A_2	τ_3	A_3
tr-PL	DCN	500	0.30 ns	0.31	1.14 ns	0.47	4.00 ns	0.22
λ_{ex} = 400 nm	DCN-0.05	500	0.22 ns	0.49	0.90 ns	0.40	3.40 ns	0.11
fs-TA	DCN	500	8.5 ± 2.0 ps	−0.53	2152 ± 500 ps	−0.47	–	–
λ_{ex} = 355 nm	DCN-0.05	500	28 ± 8 ps	−0.54	3900 ± 1200 ps	−0.46	–	–
ns-TA	DCN	430	120 ± 1 ns	0.96	7.8 ± 0.2 μs	0.04	–	–
λ_{ex} = 350 nm	DCN-0.05	430	85 ± 0.6 ns	0.91	9.2 ± 0.2 μs	0.09	–	–

[a] λ represents probed wavelength. [b] τ is referred to decay lifetime. [c] A represents amplitude of decay.

Deconvolution of the decay spectra gives the three lifetimes of charge carries as listed in Table 2. The three lifetimes of charge carriers are attributed to free polarons hopping transport of singlet excitions in intraplanar, interplanar or intrachain with following with the electron-hole recombination.[29] The population of short-lived electron-hole pairs (less than 1 ns) in the defective g-C_3N_4 is dominant resulting from the rapid recombination of photoinduced charge carriers, which is in accordance with the literatures results.[14, 30] Compared with DCN, the amplitude of short lifetimes in DCN-0.05 increases from 0.78 to 0.89, and the amplitude of the long-lived charges decreases from 0.22 to 0.11. As is well-known, PL spectra presents the information about recombination of free charges lay near band edges rather than the recombination caused by deeply trapped charges.[31] Besides, previous reports elucidated that the decay lifetimes of g-C_3N_4 shortened with the decrease of stacking distance between two adjacent layers, leading to enhanced photocatalytic activity.[30, 31b, 32] The reports above are in accordance with our tr-PL results and photocatalytic CO_2 reduction activity. Therefore, the PL results can be explained that the faster decay is attibuted the decreased layered stacking distance caused by defects in DCN-*x*. The decrease of layers stacking distance of DCN-*x* is in favor of hopping rate and mobility of electrons and holes resulting into enhanced catalytic activity.[29]

In order to analyze the mobility of charges, the transient absorption (TA) spectra were performed over six orders of magnitude in time. As shown in Figure 5a, b, the fs-TA measurements reveal a ground state bleaching signal in 400-600 nm region for both materials, which is assigned to the stimulated emission.[29-30] The decay curves for DCN and DCN-0.05 are shown in Figure 5c, d, multi-exponential decays fitting was made to yield two lifetimes spanning as listed in Table 2. The decay kinetics profiles of fs-TA spectra probed at 500 nm for DCN exhibits a short-lived (8.5 ps, −0.53) and a long-lived (2152 ps, −0.47) lifetime of charges, which are due to the photogenerated electron-hole recombination and nonradiative relaxation, respectively. Importantly, a longer lifetime of charges (28 ps and 3900 ps) was observed for DCN-0.05 (the amplitude is almost unchanged), suggesting that defect states in g-C_3N_4 act as the initial trapped states of charges, thus leading to enhanced charge separation and transport.[33]

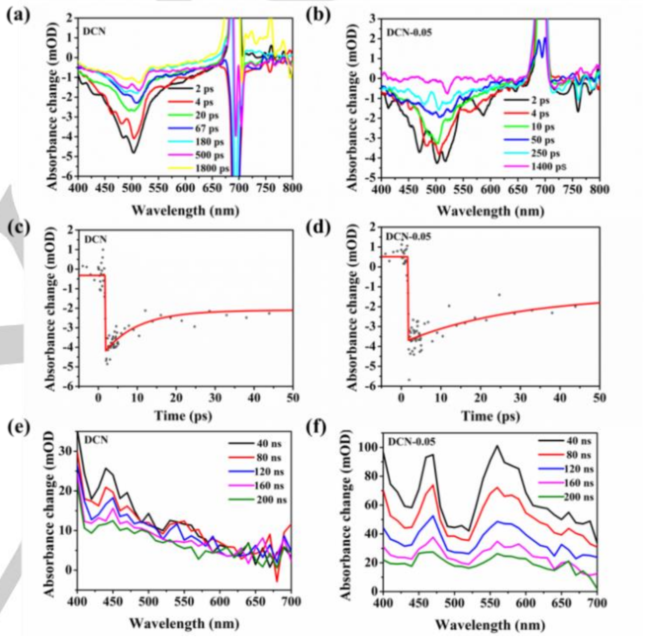

Figure 5. (a, b) fs-TA spectra. (c, d) the decay curves and fitting curves of DCN and DCN-0.05 dispersions (2 mg/mL aqueous) probed at 500 nm with 350 nm excitation. (e, f) ns-TA spectra of DCN and DCN-0.05 dispersions (0.1 mg/mL aqueous) probed at 430 nm with 355 nm excitation.

The absorption of the longer-lived charges was further measured by ns-TA spectroscopy. As shown in Figure 5e, f, ns-TA spectra for DCN present a broad positive absorption in the visible region peaking at 430 nm. Similar positive features are also observed in the DCN-0.05 ns-TA spectra, and the band is red-shifted to 460 nm and a new band at 580 nm appears. Currently, transient absorption following up to the microsecond time scale has been measured (Figure S15). The decay curves were fitted by two-exponential decay (Figure S16 and Table 2). A short-lived (120 ns, 0.96) and long-lived (7.8 μs, 0.04) lifetimes of charge carriers were obtained for DCN due to geminate recombination and bimolecular recombination, respectively. A shorter lifetime (85 ns, 0.91) and a longer lifetime (9.2 μs, 0.09) were also deteced in DCN-0.05. The population of short-lived charge carriers is dominant for both materials. Obviously, DCN-0.05 has a faster decay lifetime along with the amplitude of short lifetime decreases and the amplitude of long lifetime increases compared with DCN. This result further indicates that the decreased stacking distance is responsible for shortening of the lifetime of charges. Meanwhile, defects in the $g\text{-}C_3N_4$ could act as the trapped states of electrons or holes, which slow down the bimolecular recombination relaxation resulting in prolonging the lifetime of charge carriers.

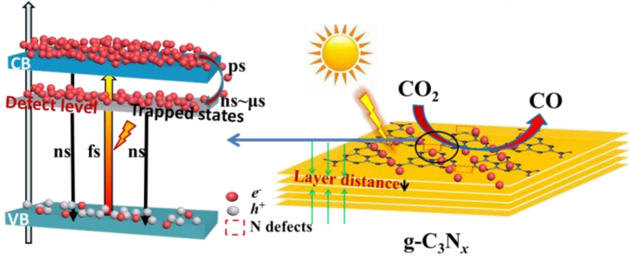

Figure 6. Schematic of dynamics process of electrons and holes photogenerated in the $g\text{-}C_3Nx$ for enhanced CO evolution driven by solar irradiation

Based on the above analysis, the energy-band configuration of $g\text{-}C_3N_x$ is drawn in Figure 6. Briefly, upon visible light excitation, hot electrons are generated, which will transfer from VB to CB of $g\text{-}C_3N_x$ and hole left in the VB (<200 fs). The initial charge carriers separate in ultrafast time scale (ps) in competition with geminate recombination and further bimolecular recombination relaxation (ns-µs) in the excited states. However, the N defects can act as charges trapped states to prolong the lifetime of both short-lived (ps) and long-lived (µs) charge carriers for further promoting charges separation. Furthernmore, the free electrons go back to the ground state (VB) resulting in photoluminescence emission (ns). The decreased layer distance attributed to faster tr-PL decay in favor of trapped electrons migrating to catalyst surface, then reacting with CO_2 molecular to produce CO. Thus, the defects act as the crucial role in trapping and separating charges to enhance photocatalytic CO_2 reduction into CO activity.

Conclusions

In summary, we successfully prepared the two-dimensional graphitic carbon nitride nanosheets with nitrogen vacancies located at both tricoordinated N atoms and uncondensed terminal NH_x species by one-step tartaric acid assistant thermal polymerization of dicyandiamide. Compared with pristine $g\text{-}C_3N_4$, the obtained $g\text{-}C_3N_x$ possessed much larger specific area and pore volume, decreased band gap, and enhanced visible light absorption as well as charge separation efficiency. Transient absorption spectra revealed that the defects in $g\text{-}C_3N_x$ acted as the trapped states of charge resulting in the prolonged lifetimes of charge carriers photoexcited. Time-resolved photoluminescence spectra analysis ensured that the faster decay of charges was attributed to the decreased layer stacking distance caused by defects in $g\text{-}C_3N_x$ in favor of hopping transition and mobility of charge carriers to surface of materials. These synergic features of the $g\text{-}C_3N_x$ nanosheets contribute to the high photocatalytic activity in CO_2 reduction driven by visible light. This work presents the crucial role of defect sites in modulating light absorption, charge separation and lifetime as well as solar CO_2 reduction efficiency, opening an avenue enabling efficient and stable solar fuel production.

Experimental Section

Fabrication of $g\text{-}C_3N_4$ and $g\text{-}C_3N_x$. Bulk $g\text{-}C_3N_4$ was prepared by thermal-polymerization of dicyandiamide. In detail, 5 g of dicyandiamide was calcined at 550ºC in a muffle furnace for 3 h with a heating rate of 5ºC min^{-1}. Nitrogen deficient $g\text{-}C_3N_4$ photocatalysts were synthesized as follows: different amount of tartaric acid (TA) (0.01-0.1g) were dissolved in 10 mL deionized water, and then 5 g dicyandiamide was added into the tartaric acid aqueous solution with stirring. The above mixture was dried in an oven at 90 ºC overnight. The resulting solid mixture was then calcined in a muffle furnace at 550ºC for 3 h with a heating rate of 5ºC min^{-1}. The products were denoted as DCN-*x* (*x* = 0.01, 0.025, 0.05, 0.075 and 0.1 corresponding to the mass (g) of tartaric acid, and DCN represents the pristine $g\text{-}C_3N_4$ synthesized by dicyandiamide).

Characterization. X-ray diffraction (XRD) patterns were recorded on a Smart Lab 9 X-ray diffractometer (Rigaku Corporation). Fourier transform infrared (FT-IR) spectra were measured using an EQUINOX55 FT-IR spectrometer. Thermogravimetric Analysis (TG) results were received on a SDT Q600 apparatus from 298 K to1073 K with a heating rate of 10 K/min in air. X-ray photoelectron spectroscopy (XPS) spectra were recorded on a Thermo VG ESCALAB250 instrument. Elemental analysis (EA) was studied on a Vario EL cube instrument (Elementar, Germany). The nitrogen adsorption isotherms were measured with a Quantachrome autosorb-iQ2 gas adsorption analyzer at 77 K. Scanning electron microscopy (SEM) images were obtained on a Hitachi SU8220 instrument with an acceleration voltage of 5 kV. Transmission electron microscopy (TEM) images were taken on a Tecnai G220 S-twin instrument (FEI Company). UV-Vis spectra were taken on a JASCO V-550 spectrometer. Photoluminescence (PL) spectra were acquired on a JASCO FP-6200 spectrofluorometer with the excitation wavelength at 310 nm. The electron paramagnetic resonance (EPR) was carried out at room temperature on an A220-9.5/12 (Bruker). Time-resolved photoluminescence (tr-PL) measurements were carried out at room temperature by the time-correlated single photon counting (TCSPC) technique (PicoQuant PicoHarp 300). By use of deconvolution/fit program (PicoQuant FluFit) the time resolution was reached down to 10 ps. The second harmonic of a titanium−sapphire laser (Mai Thai DeepSee) at 350 nm (150 fs, 80 MHz) was used as the excitation source.

Transient Absorption Spectroscopy. The transient absorption (TA) spectra were measured by optical femtosecond pump-probe spectroscopy described in detail in Ref..[34] The output of a mode-locked Ti-sapphire amplified laser system (Spitfire Ace, Spectra-Physics) with wavelength 800 nm, pulse-width 35 fs, repetition rate 1 kHz, average power 4 W was split into two beams (10:1). The strong radiation was converted into UV-VIS-IR in the range of 240-2400 nm by use of Optical Parametric Amplifier (TOPAS, Light Conversion) with 355 nm excitation and used as a pump beam. The weaker beam after passing a variable delay line (up to 6 ns) was focused in a 3 mm thickness rotated CaF2 plate to produce a white light continuum (WLC), which was used as a probe beam. Home-built pump-probe setup was used for obtaining transient absorption spectra and kinetics. The relative polarizations between pump and probe beam were set to the magic angle (54.7°) to avoid rotational depolarization effects. The entire setup was controlled by a PC with the help of LabView software (National Instruments). All measurements were performed at room temperature under aerated conditions. 2 mg/mL samples were dispersed in aqueous solution and transferred to 1 mm path length cuvettes. The experimental data were fitted to a multiexponential decay function convoluted with the instrument response function. Overall time resolution was about 20-30 fs.

Nanosecond time-resolved transient absorption spectra were recorded on a LP980 laser flash photolysis spectrometer (Edinburgh Instruments Ltd.) in combination with a Nd:YAG laser (Surelite I-10, Continuum Electro-Optics, Inc.). Samples in argon atmosphere were excited by a 355 nm laser pulse (1 Hz, 100 mJ per pulse, fwhm ≈ 7 ns) at room temperature. Concentration of samples was 0.1 mg/mL aqueous with absorbances lower than 0.5 OD at 355 nm in 1 cm path length quartz cuvettes.

Photocatalytic test. Photocatalytic CO_2 reduction experiment was conducted in a 38 mL quartz vessel with a rubber septum at the temperature of 25ºC carried out by circulation cooling system. The visible light was provided by using a 300 W Xenon lamp (PLS-SXE300C, Beijing Perfectlight Co. Ltd., China) coupled to a UV cut-off filter (λ > 400 nm). In a typical experiment, 5 mg photocatalyst was dispersed in 5 mL of solution containing 4 mL of methyl cyanide (MeCN) solvent, 1 mL of triethanolamine (TEOA), bipyridine (bpy) (10 mmol/L) and 25 μL of 20 mmol/L $CoCl_2$ aq. The mixture system was subjected to ultrasound treatment for 30 min, purged by CO_2 (99.999%) for 30 min to remove air and then was sealed. The produced gases (H_2 and CO) were detected with a syringe per hour by the gas Chromatograph equipped with TCD detector and FID detector connection in series (C molecular sieve column) methane reforming furnace. Argon was used as the carrier gas.

Photoeletrochemical test. Photoeletrochemical tests were performed on a three-electrode system using an electrochemical workstation (CHI660D, Shanghai, China). Pt and Ag/AgCl electrode were used as counter electrode and reference electrode, respectively. The samples films coated on FTO glasses (1×1 cm^2) by dip-coating method (5 mg of sample dispersed in 1mL of ethanol) was used as working electrode. A 300 W Xe lamp (λ > 400 nm) was used as the light source and Na_2SO_4 (0.2 M) as the electrolyte solution. The electrochemical impedance spectra (EIS) were recorded over a frequency range of 0.01–10^5 Hz with an amplitude of 5 mV at the same bias voltages.

Acknowledgements

This work was financially supported by the National Key Research and Development Program of China (2016YFB0600902-5).

Keywords: Nitrogen vacancies; Carbon Nitride; Transient absorption spectroscopy; Charge separation dynamics; Solar CO_2 reduction

[1] a) S. Gao, B. Gu, X. Jiao, Y. Sun, X. Zu, F. Yang, W. Zhu, C. Wang, Z. Feng, B. Ye, Y. Xie, *J. Am. Chem. Soc.* **2017**, *139*, 3438-3445; b) S. Gao, X. Jiao, Z. Sun, W. Zhang, Y. Sun, C. Wang, Q. Hu, X. Zu, F. Yang, S. Yang, *Angew. Chem. Int. Ed.* **2016**, *55*, 698-702; c) C. Song, *Catal. Today* **2006**, *115*, 2-32; d) X. Chang, T. Wang, J. Gong, *Energ. Environ. Sci.* **2016**, *9*, 2177-2196.

[2] a) S. Lin, C. S. Diercks, Y. B. Zhang, N. Kornienko, E. M. Nichols, Y. Zhao, A. R. Paris, D. Kim, P. Yang, O. M. Yaghi, *Science* **2015**, *349*, 1208-1213; b) Z. Cao, D. Kim, D. Hong, Y. Yu, J. Xu, S. Lin, X. Wen, E. M. Nichols, K. Jeong, J. A. Reimer, *J. Am. Chem. Soc.* **2016**, *138*, 8120-8125; c) D. Kim, J. Resasco, Y. Yu, A. M. Asiri, P. Yang, *Nat. Commun.* **2014**, *5*, 4948-4955; d) V. S. Thoi, N. Kornienko, C. G. Margarit, P. Yang, C. J. Chang, *J. Am. Chem. Soc.* **2013**, *135*, 14413-14424; e) H. Zhang, J. Wei, J. Dong, G. Liu, L. Shi, P. An, G. Zhao, J. Kong, X. Wang, X. Meng, *Angew. Chem. Int. Ed.* **2016**, *128*, 14522-14526; f) G. Liu, X. Meng, H. Zhang, G. Zhao, H. Pang, T. Wang, P. Li, T. Kako, J. Ye, *Angew. Chem. Int. Ed.* **2017**, *56*, 5570-5574.

[3] T. Inoue, A. Fujishima, S. Konishi, K. Honda, *Nature* **1979**, *277*, 637-638.

[4] J. Fu, B. Zhu, C. Jiang, B. Cheng, W. You, J. Yu, *Small* **2017**, *13*, 1603938-1603947.

[5] K. P. Kuhl, E. R. Cave, D. N. Abram, T. F. Jaramillo, *Energ. Environ. Sci.* **2012**, *5*, 7050-7059.

[6] X. Wang, K. Maeda, A. Thomas, K. Takanabe, G. Xin, J. M. Carlsson, K. Domen, M. Antonietti, *Nat. Mater.* **2009**, *8*, 76-80.

[7] a) X. Chen, J. Zhang, X. Fu, M. Antonietti, X. Wang, *J. Am. Chem. Soc.* **2009**, *131*, 11658-11659; b) G. Zhang, C. Huang, X. Wang, *Small* **2015**, *11*, 1215-1221; c) B. Yue, Q. Li, H. Iwai, T. Kako, J. Ye, *Sci. Technol. Adv. Mater.* **2011**, *12*, 034401-034407; d) T. Xiong, W. Cen, Y. Zhang, F. Dong, *ACS Catal.* **2016**, *6*, 2462-2472; e) Y. Wang, Y. Wang, Y. Li, H. Shi, Y. Xu, H. Qin, X. Li, Y. Zuo, S. Kang, L. Cui, *Catal. Commun.* **2015**, *72*, 24-28; f) G. Zhang, Z.-A. Lan, L. Lin, S. Lin, X. Wang, *Chem. Sci.* **2016**, *7*, 3062-3066.

[8] a) J. Zhang, M. Zhang, S. Lin, X. Fu, X. Wang, *J. Catal.* **2014**, *310*, 24-30; b) G. Zhang, M. Zhang, X. Ye, X. Qiu, S. Lin, X. Wang, *Adv. Mater.* **2014**, *26*, 805-809; c) Y. Wang, H. Li, J. Yao, X. Wang, M. Antonietti, *Chem. Sci.* **2011**, *2*, 446-450; d) K. Wang, Q. Li, B. Liu, B. Cheng, W. Ho, J. Yu, *Appl. Catal. B Environ.* **2015**, *176–177*, 44-52.

[9] a) C. Q. Xu, Y. H. Xiao, Y. X. Yu, W. D. Zhang, *J. Mater. Sci.* **2018**, *53*, 409-422; b) Z. Sun, J. M. T. A. Fischer, Q. Li, J. Hu, Q. Tang, H. Wang, Z. Wu, M. Hankel, D. J. Searles, L. Wang, *Appl. Catal. B Environ.* **2017**, *216*, 146-155; c) L. Ye, D. Wu, K. H. Chu, B. Wang, H. Xie, H. Y. Yip, P. K. Wong, *Chem. Eng. J.* **2016**, *304*, 376-383; d) P. Niu, M. Qiao, Y. Li, L. Huang, T. Zhai, *Nano Energy* **2018**, *44*, 73-81.

[10] a) G. Zhao, H. Pang, G. Liu, P. Li, H. Liu, H. Zhang, L. Shi, J. Ye, *Appl. Catal. B Environ.* **2017**, *200*, 141-149; b) J. Zhou, W. Chen, C. Sun, L. Han, C. Qin, M. Chen, X. Wang, E. Wang, Z. Su, *ACS Appl. Mater. Interfaces.* **2017**, *9*, 11689-11695; c) Q. Huang, J. Yu, S. Cao, C. Cui, B. Cheng, *Appl. Surf. Sci.* **2015**, *358*, 350-355.

[11] a) B. Long, Y. Zheng, L. Lin, K. A. Alamry, A. M. Asiri, X. Wang, *J. Mater. Chem. A* **2017**, *5*, 16179-16188; b) Y. Fukasawa, K. Takanabe, A. Shimojima, M. Antonietti, K. Domen, T. Okubo, *Chem-Asian J.* **2011**, *6*, 103-109; c) J. Zhang, F. Guo, X. Wang, *Adv. Funct. Mater.* **2013**, *23*, 3008–3014; d) L. Sun, M. Yang, J. Huang, D. Yu, W. Hong, X. Chen, *Adv. Funct. Mater.* **2016**, *26*, 4943-4950.

[12] a) Y. Zheng, L. Lin, X. Ye, F. Guo, X. Wang, *Angew. Chem. Int. Ed.* **2014**, *126*, 12120-12124; b) J. Sun, J. Zhang, M. Zhang, M. Antonietti, X. Fu, X. Wang, *Nat. Commun.* **2012**, *3*, 1139-1145; c) J. Zhang, M. Zhang, C. Yang, X. Wang, *Adv. Mater.* **2014**, *26*, 4121-4125; d) J. Wang, J. Cong, H. Xu, J. Wang, H. Liu, M. Liang, J. Gao, Q. Q. Ni, J. Yao, *ACS Sustain. Chem. Eng.* **2017**, *5*, 10633-10639; e) P. Yang, H. Ou, Y. Fang, X. Wang, *Angew. Chem. Int. Ed.* **2017**, *56*, 1-6; f) H. Ou, L. Lin, Z. Yun, P. Yang, Y. Fang, X. Wang, *Adv. Mater.* **2017**, *29*, 1700008-1700013.

[13] a) J. Ding, W. Xu, H. Wan, D. Yuan, C. Chen, L. Wang, G. Guan, W.-L. Dai, *Appl. Catal. B Environ.* **2018**, *221*, 626-634; b) X. Chen, L. Liu, P. Y. Yu, S. S. Mao, *Science* **2011**, *331*, 746-750; c) T. L. Thompson, J. T. J. Yates, *Chem. Rev.* **2006**, *38*, 4428-4453; d) P. Y. Yu, M. Cardona, *Fundamentals of semiconductors: physics and materials properties*, Springer, Heidelberg, **2010**.

[14] P. Niu, G. Liu, H. M. Cheng, *J. Phys. Chem. C* **2012**, *116*, 11013–11018.

[15] Z. Hong, B. Shen, Y. Chen, B. Lin, B. Gao, *J. Mater. Chem. A* **2013**, *1*, 11754-11761.

[16] H. Yu, R. Shi, Y. Zhao, T. Bian, Y. Zhao, C. Zhou, G. I. N. Waterhouse, L. Z. Wu, C. H. Tung, T. Zhang, *Adv. Mater.* **2017**, *29*, 1605148-1605154.

[17] P. Niu, L. C. Yin, Y. Q. Yang, G. Liu, H. M. Cheng, *Adv. Mater.* **2014**, *26*, 8046-8052.

[18] J. Ding, W. Xu, H. Wan, D. Yuan, C. Chen, L. Wang, G. Guan, W. L. Dai, *Appl. Catal. B Environ.* **2018**, *221*, 626-634.

[19] S. Samanta, R. Srivastava, *Sustain. Energ. Fuels* **2017**, *1*, 1390-1404.

[20] L. Ye, D. Wu, K. H. Chu, B. Wang, H. Xie, H. Y. Yip, P. K. Wong, *Chem. Eng. J.* **2016**, *304*, 376-383.

[21] A. Thomas, A. Fischer, F. Goettmann, M. Antonietti, J. O. Mueller, R. Schloegl, J. M. Carlsson, *Cheminform* **2009**, *40*, 4893-4908.

[22] P. Niu, L. Zhang, G. Liu, H. M. Cheng, *Adv. Funct. Mater.* **2012**, *22*, 4763–4770.

[23] S. Yang, Y. Gong, J. Zhang, L. Zhan, L. Ma, Z. Fang, R. Vajtai, X. Wang, P. M. Ajayan, *Adv. Mater.* **2013**, *25*, 2452-2456.

[24] a) J. Ding, W. Xu, H. Wan, D. Yuan, C. Chen, L. Wang, G. Guan, W. L. Dai, *Appl. Catal. B Environ.* **2018**, *221*, 626-634; b) N. Sun, Y. Liang, X. Ma, F. Chen, *Chem. Eur. J* **2017**, *23*, 1-9.

[25] L. J. Fang, X. L. Wang, J. J. Zhao, Y. H. Li, Y. L. Wang, X. L. Du, Z. F. He, H. D. Zeng, H. G. Yang, *Chem. Commun.* **2016**, *52*, 14408-14411.

[26] S. Trasatti, *Pure Appl. Chem.* **1986**, *58*, 955-966.

[27] G. Liu, G. Zhao, W. Zhou, Y. Liu, H. Pang, H. Zhang, D. Hao, X. Meng, P. Li, T. Kako, *Adv. Funct. Mater.* **2016**, *26*, 6822-6829.

[28] G. Dong, W. Ho, C. Wang, *J. Mater. Chem. A* **2015**, *3*, 23435-23441.

[29] C. Merschjann, S. Tschierlei, T. Tyborski, K. Kailasam, S. Orthmann, D. Hollmann, T. Schedel-Niedrig, A. Thomas, S. Lochbrunner, *Adv. Mater.* **2015**, *27*, 7993-7999.

[30] R. Godin, Y. Wang, M. A. Zwijnenburg, J. Tang, J. R. Durrant, *J. Am. Chem. Soc.* **2017**, *139*, 5216-5224.

[31] a) F. Vietmeyer, P. A. Frantsuzov, B. Janko, M. Kuno, *Phys. Rev. B* **2011**, *83*, 115319-115328; b) C. Merschjann, T. Tyborski, S. Orthmann, F. Yang, K. Schwarzburg, M. Lublow, M. C. Lux-Steiner, T. Schedel-Niedrig, *Phys. Rev. B* **2013**, *87*, 205204-205211; c) A. R. Srimath Kandada, S. Neutzner, V. D'Innocenzo, F. Tassone, M. Gandini, Q. A. Akkerman, M. Prato, L. Manna, A. Petrozza, G. Lanzani, *J. Am. Chem. Soc.* **2016**, *138*, 13604-13611.

[32] H. Zhang, A. Yu, *J. Phys. Chem. C* **2014**, *118*, 11628-11635.

[33] D. J. Martin, K. Qiu, S. A. Shevlin, A. D. Handoko, X. Chen, Z. Guo, J. Tang, *Angew Chem Int Ed Engl* **2015**, *53*, 9240-9245.

[34] X. Li, C. Gong, G. G. Gurzadyan, M. F. Gelin, J. Liu, L. Sun, *J. Phys. Chem. C* **2017**, *122*, 50-61.

10.1002/chem.201805923

Table of Contents

FULL PAPER

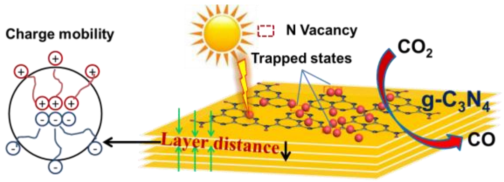

Rich nitrogen defects in $g\text{-}C_3N_4$ were achieved by one-step tartaric acid assistant thermal polymerization of dicyandiamide. The defects in $g\text{-}C_3N_4$ act as the charge trapped states to prolong the lifetime of charge carriers. The decreased layer distance caused by nitrogen vacancies is in favor of charge transport and mobility to surface of catalyst. Deficient $g\text{-}C_3N_4$ exhibits the enhanced photocatalytic CO_2 reduction activity.

Hainan Shi,[a] Saran Long,[a] Jungang Hou,[a], Lu Ye,[a] Yanwei Sun,[a] Wenjun Ni,[a] Chunshan Song,[a,b] Keyan Li,*[a], Gagik G.Gurzadyan[a] and Xinwen Guo*[a]*

Page No.1 – Page No.8

Defects Promoting Ultrafast Charge Separation in Graphitic Carbon Nitride Enhanced Visible-Light-Driven CO_2 Reduction Activity